




## Insights into the facet- and direction-dependent photoelectric properties of anatase and rutile TiO<sub>2</sub>

Jiali Jiang, Xiangchao Ma <sup>\*</sup>, Haojiang Fan, Xin Wu, and Delian Liu   
*School of Optoelectronic Engineering, Xidian University, Xi'an, 710071, China*

 (Received 15 September 2023; revised 2 April 2024; accepted 14 May 2024; published 28 May 2024)

In general, the photoelectric properties of TiO<sub>2</sub> are highly dependent on its crystal directions and facets. However, the impact of initial momentum distributions, group velocity distributions, and spatial transport properties of photoexcited carriers on the anisotropic photoelectric properties needs more study. In this work, we have thoroughly investigated these issues at the atomic and electronic scales for anatase and rutile TiO<sub>2</sub> with homemade code. It is meaningful to find that anatase and rutile TiO<sub>2</sub> mainly produce high-energy electrons and holes upon photoexcitation, respectively, which is beneficial for the efficient separation of carriers in the heterojunction system of anatase and rutile TiO<sub>2</sub>. In addition, it is found that for both anatase and rutile TiO<sub>2</sub>, the initial momentum and group velocity distribution of the photoexcited carriers is highly anisotropic, and anatase TiO<sub>2</sub> has a better directionality than rutile as a whole. Moreover, the transport properties of carriers in group velocity space also exhibit high anisotropy. Notably, the crystal directions with excellent transport properties are consistent with the group velocity distribution of carriers in anatase TiO<sub>2</sub>, which indicates the beneficial transport and accumulation of photoexcited carriers. In contrast, the crystal directions with excellent transport properties are inconsistent with the preferable group velocity distribution of carriers in rutile TiO<sub>2</sub>, which may result in unfavorable carrier transport and accumulation properties. These results provide not only valuable thoughts for understanding related experimental phenomena but also theoretical guidance for effectively collecting carriers in TiO<sub>2</sub>.

DOI: [10.1103/PhysRevB.109.205207](https://doi.org/10.1103/PhysRevB.109.205207)

### I. INTRODUCTION

Semiconductor materials are crucial for photoelectric applications [1–3]. Among many candidate semiconductor materials, titanium dioxide (TiO<sub>2</sub>) is one of many potential semiconductors that has found widespread use in photocatalysis, photoelectrocatalysis, sensing, and photovoltaics due to its favorable band-edge locations, high electron transport efficiency, long-term photochemical stability, and nontoxicity [4–8]. Anatase, rutile, and brookite are the three main phases of TiO<sub>2</sub> in nature. Among them, anatase and rutile TiO<sub>2</sub> have attracted much interest in both fundamental research and industrial applications due to their stability and high photoelectric performance [1,9,10].

In general, the photoelectric properties of TiO<sub>2</sub> are highly dependent on its facet and crystal direction. For example, most of the works show that the (101) and (001) facets of anatase TiO<sub>2</sub> have higher photoelectric activity; electrons mainly accumulate to the (101) facets, and holes to the (001) facets [11–15]. In addition, some studies indicate that anatase TiO<sub>2</sub> with a higher proportion of (001) does not always have higher photocatalytic activity [16,17]. The rutile TiO<sub>2</sub> also has such obvious facet-dependent photoelectric activities. For example, (110) facets of rutile TiO<sub>2</sub> have a higher level of photoelectric activity than (111) facets, and (001) facets show stronger oxidation power than that of the (111) facets [18–20]. In order to explain the phenomenon of the facet-dependent results, many

researchers have proposed possible mechanisms. Zhang *et al.* investigated the electronic structures and effective mass of anatase, rutile, and brookite TiO<sub>2</sub>, and revealed the connection between the anisotropy of the effective mass of carriers and the different crystal facet activities [21]. Di Liberto *et al.* [22] as well as others suggest that (101) and (001) facets have different surface energetics, which can cause electric potential differences (band bending), thus permitting electrons and holes to transfer to different crystal facets [6,14,15,22]. Using the TiO<sub>2</sub> cluster model, Li and Liu [23] as well as others show that its highest occupied orbit (HOMO) and lowest unoccupied orbit (LUMO) locate on the facets of (001) and (101), respectively, thereby causing reduction reactions on the (101) facets and oxidation reactions on the (001) facets [23,24]. From the perspective of specific facet chemistry and kinetics, Selcuk and Selloni [25] and Heiz and co-workers [26] report that the electron trapping features of different facets of anatase TiO<sub>2</sub> depend strongly on the surrounding environment and the nature of electron donors. As can be seen, almost all the previous studies mainly focus on the physical and chemical properties of the surface, to understand the dependence of photoelectric performance on crystal facets. Theoretically, the initial momentum distributions and spatial transport properties of the photoexcited carriers can also affect the accumulation of carriers on different facets. However, up until now, these factors have not been studied at the atomic and electronic scales.

In this paper, based on first-principles calculations and many-body perturbation theory, we perform systematic studies on the optical generation, initial energy distributions,

\*xcma@xidian.edu.cn

initial momentum and group velocity distributions, and spatial transport properties of carriers for both anatase and rutile  $\text{TiO}_2$ . We find that for both anatase and rutile, the initial momentum and group velocity distributions of the photoexcited carriers are highly anisotropic, and anatase has a stronger directionality than rutile as a whole. Moreover, the crystal directions with excellent transport properties are consistent with the group velocity distribution in anatase  $\text{TiO}_2$ , which indicates beneficial transport and accumulation of photoexcited carriers. In contrast, the crystal directions with excellent transport properties are inconsistent with the group velocity distribution in rutile  $\text{TiO}_2$ , which may result in unfavorable transport and accumulation properties. Our study provides unique microscopic insights into the different photoelectric properties of  $\text{TiO}_2$  facets that are beyond the scope of experiments, which deepens the understanding of the physical and photoelectric properties of anatase and rutile  $\text{TiO}_2$ .

## II. COMPUTATIONAL METHODS

### A. Electronic and phononic properties

Firstly, the electronic structure, phonon spectrum, and electron-phonon matrix elements are calculated from first principles using density functional theory (DFT) as applied by the open-source code JDFTX software [27]. We use full-relativistic norm-conserving pseudopotentials, the generalized gradient approximation functional of Perdew, Burke, and Ernzerhof (PBE) for describing the exchange-correlation energy and truncated Coulomb interactions. Fermi-Dirac smearing is 0.01 hartree and the plane-wave cutoff energy is 30 hartrees. For the accurate density of states (DOS) calculations, a dense  $27 \times 27 \times 27$  ( $18 \times 18 \times 36$ )  $k$ -point mesh is utilized for anatase (rutile)  $\text{TiO}_2$ . A  $9 \times 9 \times 9$  ( $6 \times 6 \times 12$ )  $k$ -point mesh in the Brillouin zone of anatase (rutile)  $\text{TiO}_2$  is used during structural and electronic properties calculations. Phonon calculations employ a  $3 \times 3 \times 3$  ( $2 \times 2 \times 4$ ) supercell for anatase (rutile)  $\text{TiO}_2$ . Each of the parameters above has been put to the test with well-converged results. Then, using maximally localized Wannier function (MLWF) basis representation [28], all electron, phonon, and electron-phonon matrix elements acquired by DFT are converted, respectively, and interpolated to extremely fine electron wave-vector  $k$  and phonon wave-vector  $q$  meshes. In particular, we use the 38 and 35 Wannier bands for anatase and rutile  $\text{TiO}_2$ , respectively, to precisely reproduce the electron-phonon matrix elements, phonon energies, and orbital energies. The subsequent calculations employ electron and phonon occupation factors at room temperature,  $T = 298$  K.

### B. Optical and transport properties

We develop some codes to systematically evaluate the optical response and transport properties of anatase and rutile  $\text{TiO}_2$  by Monte Carlo Brillouin-zone integration and point group transformation. Firstly, by applying MLWF to the  $k$  point in the Brillouin zone, we obtain the corresponding electronic energies, phonon energies, momentum matrix elements, and electron-phonon matrix elements. Then we evaluate the single integral over the Brillouin zone in Eq. (1) by Monte

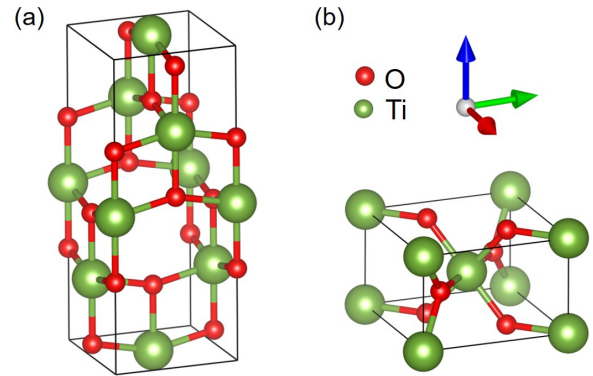


FIG. 1. The schematic conventional unit cells for anatase (a), and rutile (b)  $\text{TiO}_2$ . The green and red spheres represent Ti and O atoms, respectively.

Carlo sampling of  $1.5 \times 10^5$  ( $1.0 \times 10^5$ )  $k$  points in the Brillouin zone and evaluate the double integral over the Brillouin zone in Eq. (2) by Monte Carlo sampling of  $2.25 \times 10^6$  ( $1.0 \times 10^6$ )  $(k, k')$  pairs for anatase (rutile)  $\text{TiO}_2$ . For the transport properties, in Eqs. (6) and (7), the electronic states, phonon modes, and electron-phonon matrix elements are computed with the same method as for the optical properties; the lowest-order scattering self-energies for electron-electron and electron-phonon scattering are calculated with intensive sampling of  $14 \times 14 \times 14$  ( $12 \times 12 \times 24$ )  $k$  points and  $2.5 \times 10^4$  ( $3.0 \times 10^4$ )  $k'$  points to sufficiently resolve the summation in the Brillouin zone for anatase (rutile)  $\text{TiO}_2$ . All the parameters mentioned above have been tested to give converged results with negligible errors.

## III. RESULTS AND DISCUSSION

### A. Geometric and electronic structures

The conventional unit cells of optimized anatase and rutile  $\text{TiO}_2$  are shown in Fig. 1. The space groups of anatase and rutile  $\text{TiO}_2$  are  $I4_1/amd$  and  $P4_2/mmm$ , respectively. The calculated lattice parameters (anatase:  $a = 3.80$  Å,  $c = 9.59$  Å) and (rutile:  $a = 4.53$  Å,  $c = 2.92$  Å) are in good agreement with the experimental measurements [29,30]. In order to clarify the electronic properties of anatase and rutile  $\text{TiO}_2$ , Fig. 2 shows the band structures, density of states (DOS), and projected density of states (PDOS) of anatase and rutile  $\text{TiO}_2$ . The band structures of anatase are calculated along  $Z-\Gamma-X-P-N-\Gamma$  in the irreducible Brillouin zone (IBZ), and the band structures of rutile calculated along  $Z-\Gamma-M-X-\Gamma-Z-R$  in the IBZ. The valence band maximum (VBM), shown by a dashed line in Figs. 2(a) and 2(c), is set to 0 eV. For anatase, an indirect band gap of 2.15 eV is observed between the conduction band minimum (CBM) at the  $\Gamma$  point and the valence band maximum (VBM) near the  $X$  point. A direct band gap of about 2.5 eV is observed near the  $\Gamma$  point. For rutile, a direct band gap of 2.0 eV is observed at the  $\Gamma$  point. The calculated band characteristics are similar to previous results [21,31,32].

The lattice parameters and band gap of anatase and rutile  $\text{TiO}_2$  obtained from the DFT calculation and experiment results are summarized in Table I. For anatase, our optimized lattice parameters are consistent with the previously reported

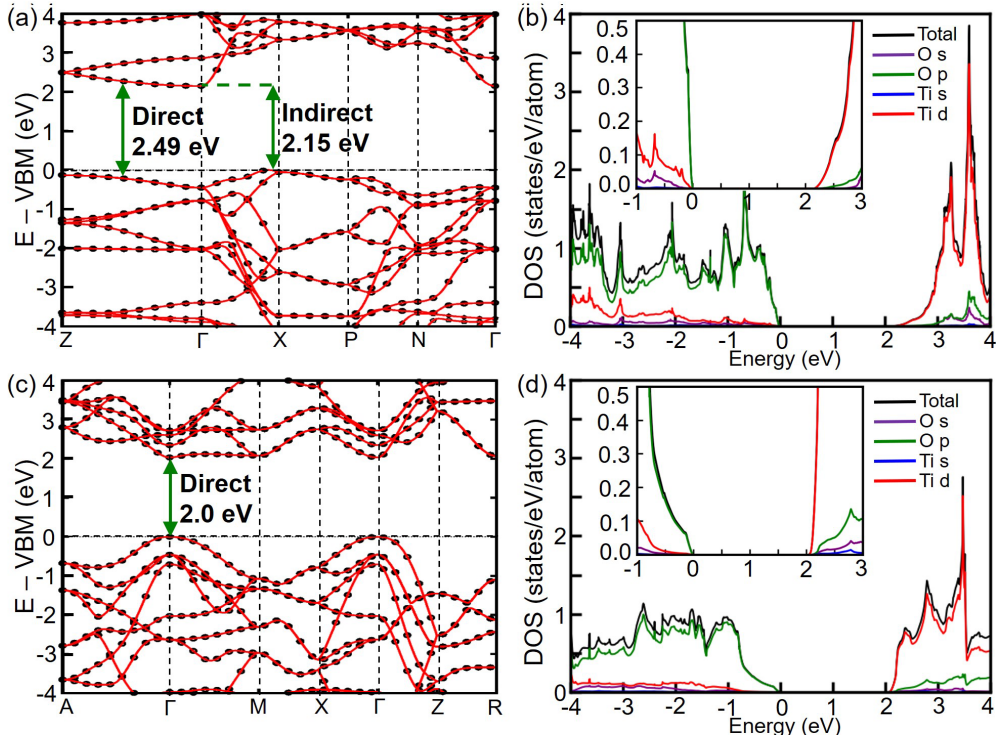


FIG. 2. Band structures of anatase (a) and rutile (c)  $\text{TiO}_2$ ; the black scatters represent band structures calculated by DFT, and the red lines are obtained by MLWF interpolation; the valence band maximum (VBM) is set to 0 eV. Total and projected density of states (DOS) of anatase (b) and rutile (d)  $\text{TiO}_2$ .

result, so the calculated band gap is also consistent with the previous report; for rutile, our optimized lattice parameters ( $a$  and  $b$ ) are smaller (1%–2%) than previously reported results, so the calculated band gap also differs from the previously reported results. The reasons for the difference in optimized lattice parameters may be as follows: on the one hand, previously reported results were calculated using VASP or CASTEP, whereas this article uses JDFTX. Due to the different pseudopotential files used in VASP (projector augmented wave method) and JDFTX (norm-conserving pseudopotentials), the optimized lattice parameters are slightly different from each other. On the other hand, the intrinsic structural characteristics of anatase and rutile may lead to this difference in optimized lattice parameters.

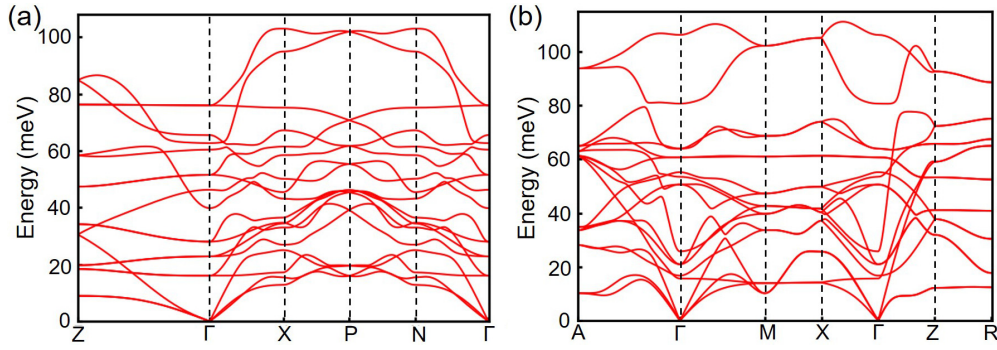
In Figs. 2(a) and 2(c), the scatters marked by black triangles show the band structures directly calculated by DFT with discrete  $k$ -point sampling in the IBZ, and the red curves show the band structures calculated by MLWF interpolation, which coincides with the scatters and provides an accurate basis for

the next calculations. As shown in Figs. 2(b) and 2(d), anatase and rutile  $\text{TiO}_2$  have similar PDOS compositions, which is in excellent agreement with previous calculations [32]. The valence bands primarily consist of O 2p states and a few Ti 3d states, indicating the strong  $p-d$  hybridizations between O 2p and Ti 3d states, which broaden the valence bands and promote the transfer of photoexcited holes. The conduction bands are mainly contributed by Ti 3d states, mixed with a few O 2p and Ti 3p states, and strong hybridization also appears between Ti 3d and O 2p states. As shown in Fig. 2(a), anatase has a relatively weak dispersion near the edge of the valence band, and the dispersion is anisotropic near the conduction band edge. Along the  $\Gamma$ -X direction, corresponding to the [110] crystal direction, it has a strong dispersion, which facilitates carrier migration. As shown in Fig. 2(c), rutile has a relatively strong dispersion near the valence band edge, and the dispersion is also anisotropic near the conduction band edge. Along the  $\Gamma$ -A and  $\Gamma$ -Z directions, corresponding to the [111] and [001] crystal directions, there is also strong dis-

TABLE I. Comparison of calculated parameter values with those in references.

Method	Anatase				Rutile			
	$a$ (Å)	$b$ (Å)	$c$ (Å)	Band gap (eV)	$a$ (Å)	$b$ (Å)	$c$ (Å)	Band gap (eV)
Expt [29,30]	3.80	3.80	9.44	3.20	4.60	4.60	2.96	4.60
DFT-PBE [33]	3.78	3.78	9.51	1.94	4.59	4.59	2.96	4.60
DFT-PBE [21]	3.80	3.80	9.70	2.13	4.64	4.64	2.97	4.64
DFT-PBE [34]					4.65	4.65	2.97	4.65
DFT-PBE (this work)	3.80	3.80	9.59	2.15	4.53	4.53	2.92	4.53



FIG. 3. Phonon dispersions of anatase (a) and rutile (b) TiO<sub>2</sub>.

persion. Figure 3 compares phonon dispersions of rutile and anatase TiO<sub>2</sub>. The calculated phonon dispersions are in good agreement with other calculations [35,36]. All the phonon modes have no imaginary frequencies, proving the dynamic stabilities of anatase and rutile TiO<sub>2</sub>.

### B. Photoexcited carrier generation rates

Efficient and wide-range optical absorption are essential conditions for the high-efficiency generation of carriers. In order to completely quantify the generation of carriers, we compute the relative contributions of direct interband and indirect phonon-assisted electronic transitions to the generation of carriers. According to the perturbation theory and Fermi's "golden rule," the imaginary part of the dielectric function

(IPDF) is calculated by Eq. (1) [37] for direct interband electronic transitions,

$$\text{Im}\varepsilon_{\text{direct}}(\omega) = \frac{4\pi^2 e^2}{3m_e^2 \omega^2 \Omega} \int_{\text{BZ}} \frac{2d\mathbf{k}}{V_{\text{BZ}}} \sum_{nn'} [f_{n\mathbf{k}}(T) - f_{n'\mathbf{k}}(T)] \times \delta(E_{n'\mathbf{k}} - E_{n\mathbf{k}} - \hbar\omega) |\langle P \rangle_{n'n}^{\mathbf{k}}|^2, \quad (1)$$

where  $E_{n\mathbf{k}}$  and  $f_{n\mathbf{k}}$  are the Kohn-Sham energy and Fermi occupations of the electronic state with wave vectors  $\mathbf{k}$  and band index  $n$ , respectively;  $|\langle P \rangle_{n'n}^{\mathbf{k}}|$  is the momentum matrix element;  $V_{\text{BZ}}$  is the volume of the Brillouin zone;  $m_e$  is the electron rest mass;  $\omega$  is the frequency of incident light; and  $\hbar\omega$  is the incident photon energy.

For phonon-assisted electronic transitions, according to second-order perturbation theory [38] and first-principles calculations, we calculate the IPDF by Eq. (2) [39–41],

$$\hat{\lambda} \text{Im}\varepsilon_{\text{phonon}} \hat{\lambda}(\omega) = \frac{4\pi^2 e^2}{\omega^2} \int_{\text{BZ}} \frac{d\mathbf{k}' d\mathbf{k}}{(2\pi)^6} \sum_{n'n'\alpha\pm} [f_{n\mathbf{k}}(T) - f_{n'\mathbf{k}'}(T)] \left[ n_{\mathbf{k}'-\mathbf{k},\alpha}(T) + \frac{1}{2} \mp \frac{1}{2} \right] \delta(E_{n'\mathbf{k}'} - E_{n\mathbf{k}} - \hbar\omega \mp \hbar\omega_{\mathbf{k}'-\mathbf{k},\alpha}) \times \left| \hat{\lambda} \sum_m \left( \frac{g_{n'\mathbf{k}',m\mathbf{k}}^{\mathbf{k}'-\mathbf{k},\alpha} \langle \mathbf{P} \rangle_{mn}^{\mathbf{k}}}{E_{m\mathbf{k}} - E_{n\mathbf{k}} - \hbar\omega + i\eta} + \frac{\langle \mathbf{P} \rangle_{n'm}^{\mathbf{k}'} g_{m\mathbf{k}',n\mathbf{k}}^{\mathbf{k}'-\mathbf{k},\alpha}}{E_{m\mathbf{k}'} - E_{n\mathbf{k}} \mp \hbar\omega_{\mathbf{k}'-\mathbf{k},\alpha} + i\eta} \right) \right|^2, \quad (2)$$

where  $\hbar\omega_{\mathbf{k},\alpha}$  and  $n_{\mathbf{k},\alpha}$  are the energy and Bose occupations of the phonon state with wave vector  $\mathbf{k}$  and polarization index  $\alpha$ , respectively;  $\hat{\lambda}$  is a test unit vector along the field direction;  $g_{m\mathbf{k}',n\mathbf{k}}^{\mathbf{k}'-\mathbf{k},\alpha}$  is the electron-phonon matrix element. The sum over  $\pm$  accounts for phonon absorption and emission;  $\eta$  is a small Lorentzian broadening, which is set to 0.1 eV.

The IPDF at different photon energies is related to the generation rate of photoexcited carriers. The higher the IPDF is, the larger the generation rate of photoexcited carriers will be. In addition, the IPDF depends to a large extent on energy. Figure 4(a) shows the IPDF as a result of the interband electronic transitions for anatase and rutile TiO<sub>2</sub>. As can be seen, the IPDFs for both anatase and rutile TiO<sub>2</sub> are almost equal to 0 at photon energies less than 2.5 and 2.0 eV, which is consistent with their band structures. At the energy range between 2.5 and 2.8 eV, the IPDF of anatase TiO<sub>2</sub> is greater than rutile TiO<sub>2</sub>, but when the energy is higher than 2.8 eV, the IPDF of anatase is significantly smaller than rutile. In addition, the IPDF for both anatase and rutile TiO<sub>2</sub> as a function of

energy is highly similar to the previous results [42–44], which confirms the reliability of our theoretical results. Overall, when the photon energy is below 2.8 eV, anatase has a higher photoexcited carrier generation rate; when the photon energy is larger than 2.8 eV, the photoexcited carrier generation rate of rutile is significantly larger than that of anatase.

Figure 4(b) shows the IPDF due to phonon-assisted indirect electronic transitions for anatase and rutile TiO<sub>2</sub>. The IPDFs of anatase and rutile TiO<sub>2</sub> are almost equal to 0 at energy less than 2.15 and 2.0 eV, respectively, which is consistent with their band structures. The IPDF values for both anatase and rutile TiO<sub>2</sub> are almost the same in the energy range below 2.8 eV. In the energy range above 2.8 eV, the IPDF values of anatase and rutile TiO<sub>2</sub> increase gradually, and the IPDF values of rutile are significantly larger than that of anatase. Overall, the IPDF of both anatase and rutile TiO<sub>2</sub> originating from phonon-assisted indirect electronic transitions is very small, which is about two orders of magnitude smaller than the IPDF of direct interband electronic transitions. Therefore,



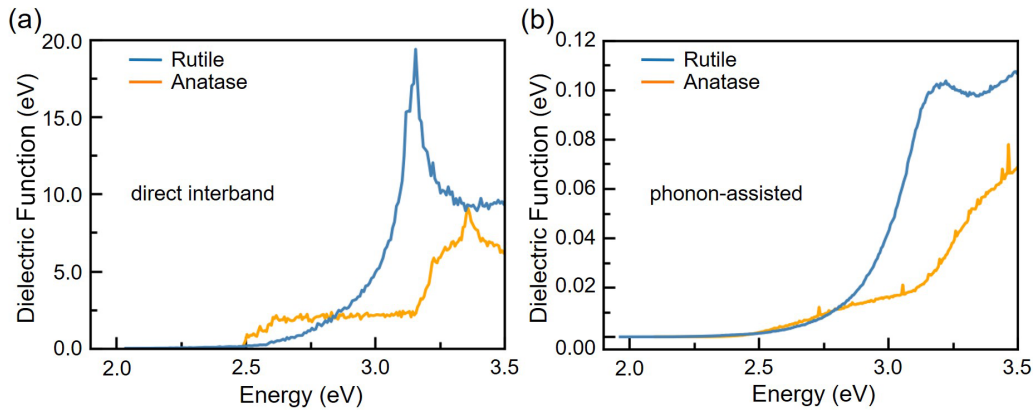


FIG. 4. The IPDF for anatase and rutile  $\text{TiO}_2$  due to direct interband electronic transitions (a) and phonon-assisted indirect electronic transitions (b).

it can be concluded that the contribution of phonon-assisted electronic transitions to the photoexcited carrier generation in these two materials can be ignored. In the following discussion, we only consider the effect of direct interband electronic transitions.

The generation rate of photoexcited carriers can be further reflected through the light absorption coefficients. The IPDF  $\varepsilon_2(\omega)$  due to direct interband electronic transitions is obtained from Eq. (1), and the real part of the dielectric function  $\varepsilon_1(\omega)$  is obtained by Kramers-Kronig transformation [45]. Finally, the optical absorption coefficient  $\alpha(\omega)$  is calculated by Eq. (3) (where  $c$  is the speed of light in vacuum and  $\omega$  is the frequency of the photon) [46,47]:

$$\alpha(\omega) = \sqrt{2} \frac{\omega}{c} \left[ \sqrt{\varepsilon_1^2(\omega) + \varepsilon_2^2(\omega)} - \varepsilon_1(\omega) \right]^{1/2}. \quad (3)$$

As shown in Fig. 5, The absorption coefficients for both anatase and rutile  $\text{TiO}_2$  increase with the increase of photon energy, and the initial absorption edges of anatase and rutile  $\text{TiO}_2$  are located at 2.49 and 2.0 eV, respectively, corresponding to 498 and 620 nm, which correspond to their direct band gap values. In the energy range of 2.5–2.8 eV, the  $\alpha(\omega)$  of anatase is larger than rutile, whereas in the energy range of 2.8–3.5 eV, the situation is just the opposite. The trend for

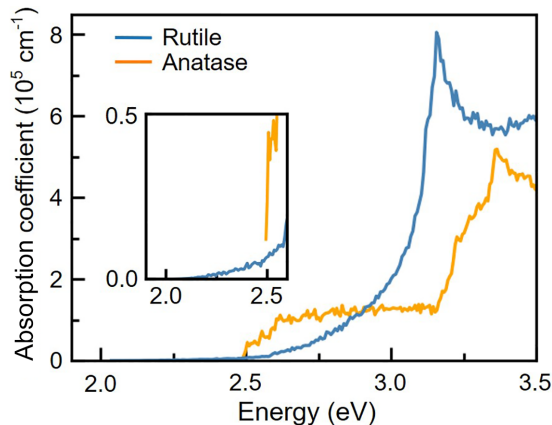


FIG. 5. The trend for the optical absorption spectra of anatase and rutile  $\text{TiO}_2$  due to direct interband electronic transitions.

the optical absorption spectra of anatase and rutile  $\text{TiO}_2$  from our theoretical calculations is consistent with the experimental measurements [32,48].

### C. Distribution of the photoexcited carriers in energy space

In practical nanoscale applications, the transport of carriers is often quasiballistic. Therefore, the initial energy distribution of photoexcited electrons and holes is crucial for their collection and utilization [37]. According to the specific physical process of photoexcited carrier generation, we analyze the energy distribution of photoexcited electrons and holes from direct interband electronic transitions, which is calculated by histogramming the integrands in Eq. (1) [39] by the initial (hole) and final (electron) state energies.

As shown in Fig. 6, the photoexcited carrier distribution in anatase and rutile  $\text{TiO}_2$  is plotted as a function of both

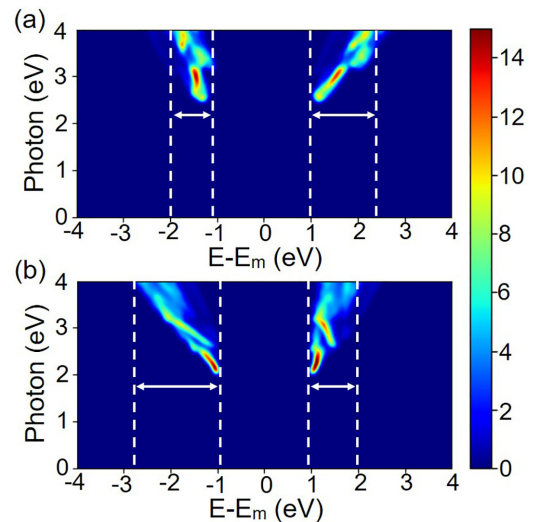


FIG. 6. The energy distribution of photoexcited carriers generated by direct interband electronic transitions for anatase (a) and rutile (b)  $\text{TiO}_2$ . The panels show the energy distribution of photo-generated hot electrons (positive energies relative to the middle of the band gap) and hot holes (negative energies) for various photon excitations. The color bar indicates the distribution probabilities of carriers.  $E_m$  indicates the middle of the band gap.

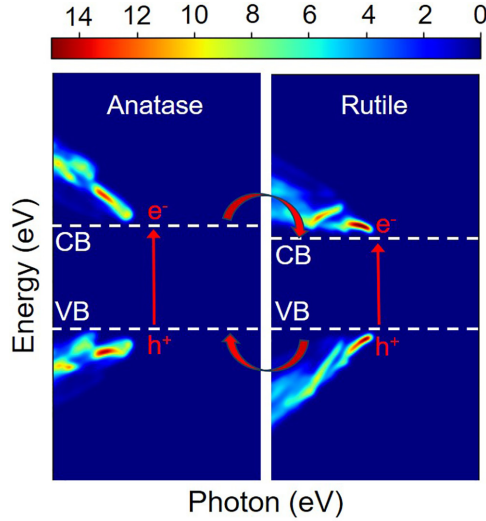


FIG. 7. The photoexcited carrier energy distributions in anatase and rutile  $\text{TiO}_2$  are plotted as functions of both photoexcited carrier energy (vertical axis) and incident photon energy (horizontal axis). The color bar indicates the distribution probabilities of carriers.

photoexcited carrier energy (horizontal axis) and incident photon energy (vertical axis). The photoexcited carriers with energies from 1 to 4 eV on the horizontal axis represent the photoexcited electrons in the conduction band and from  $-4$  to  $-1$  eV on the horizontal axis represents the photoexcited holes in the valence band. The color scale represents the distribution probabilities of photoexcited electrons and holes. The thresholds of photon energy are about 2.5 and 2.0 eV for anatase and rutile  $\text{TiO}_2$ , respectively, which is consistent with the calculated optical band gaps. When the photon energy is greater than the threshold value, the distribution of photoexcited electrons and holes of anatase and rutile  $\text{TiO}_2$  is highly localized in the energy space. With the increase of incident photon energy, the photoexcited carrier energy of anatase and rutile  $\text{TiO}_2$  gradually increases. Moreover, as indicated by the double arrow segment between the vertical dashed lines in Fig. 6, for anatase  $\text{TiO}_2$ , when incident photon energy increases from 2.5 to 4 eV, the energy distribution of photoexcited electrons is wider than that of the holes, with electrons covering about 1.4 eV and holes covering about 0.9 eV. Therefore, the proportion of high-energy electrons generated is higher than that of holes. The situation for rutile  $\text{TiO}_2$  is exactly the opposite.

Additionally, it is often acknowledged that the relative relationship of electrons within the conduction band (CB) and valence band (VB) can be quite accurately described by DFT calculations; for the band gap, it is often underestimated owing to the well-known shortcoming of the GGA functional in DFT calculations [12,49]. Our discussions of the energy space and momentum space distributions of carriers are mainly based on the internal electronic structures of conduction band and valence band edges, rather than the band gap. As shown in Fig. 7, according to the experimental results, the valence band edges of anatase and rutile  $\text{TiO}_2$  are close to each other, and the conduction band edge of rutile is 0.2 eV lower than that of anatase [49,50]. Notably,

in practical nanoscale applications, the transport of carriers is often quasiballistic, meaning that carriers can reach the surface without losing energy. Therefore, according to the experimental band alignment and the present results of energy distribution of photoexcited carriers, there should be a certain relationship between the initial energy of carriers and their corresponding reduction/oxidation ability. On the whole, anatase  $\text{TiO}_2$  mainly produces high-energy electrons with stronger reduction ability, whereas rutile  $\text{TiO}_2$  mainly produces high-energy holes with stronger oxidation ability. Furthermore, in the heterojunction of anatase and rutile  $\text{TiO}_2$ , some of the high-energy electrons produced by anatase  $\text{TiO}_2$  may transfer to the conduction band of rutile  $\text{TiO}_2$ , and some high-energy holes produced by rutile  $\text{TiO}_2$  may transfer to the valence band of anatase  $\text{TiO}_2$ ; the recombination of photoexcited carriers is thus effectively restrained. This may further explain that the heterojunction system of anatase and rutile  $\text{TiO}_2$  exhibits better photoelectric activity than that of a single system.

#### D. Distribution of photoexcited carriers in momentum and group velocity space

The anisotropic effective mass of photoexcited carriers and diverse electronic structures can result in different photoelectric properties along different directions, resulting in various optoelectronic properties on different facets [14,51]. The momentum space and group velocity space distribution of photoexcited carriers may also result in different photoelectric properties on different facets. In this section, we characterize the momentum and group velocity distribution of photoexcited carriers and discuss their potential effects on photoelectric properties. It should be noted that, for semiconductors, the electrons and holes generated by optical excitation will quickly relax to the energy states near the conduction and valence band edge, respectively. Therefore, we characterize the initial momentum distribution of energy states located near the conduction and valence band edge of the ground state electronic structure of  $\text{TiO}_2$  (within 0.2 eV). To make the discussion more comprehensive, we also characterize the momentum and group velocity distribution of energy states within the energy range of 0.4 eV about the conduction and valence band edges.

In general, the relation between the energy of the carrier and the wave vector near the band edges can be approximately described by Eq. (4). The carrier migration directions should be discussed in the group velocity space, which is defined by Eq. (5):

$$E(\vec{k}) \approx E_0 + \frac{\hbar^2}{2m_x^*} (\vec{k}_x - \vec{k}_{0,x})^2 + \frac{\hbar^2}{2m_y^*} (\vec{k}_y - \vec{k}_{0,y})^2 + \frac{\hbar^2}{2m_z^*} (\vec{k}_z - \vec{k}_{0,z})^2, \quad (4)$$

$$\vec{v} = \frac{1}{\hbar} \nabla_{\vec{k}} E(\vec{k}) \approx \frac{\hbar}{m_x^*} (\vec{k}_x - \vec{k}_{0,x}) + \frac{\hbar}{m_y^*} (\vec{k}_y - \vec{k}_{0,y}) + \frac{\hbar}{m_z^*} (\vec{k}_z - \vec{k}_{0,z}), \quad (5)$$

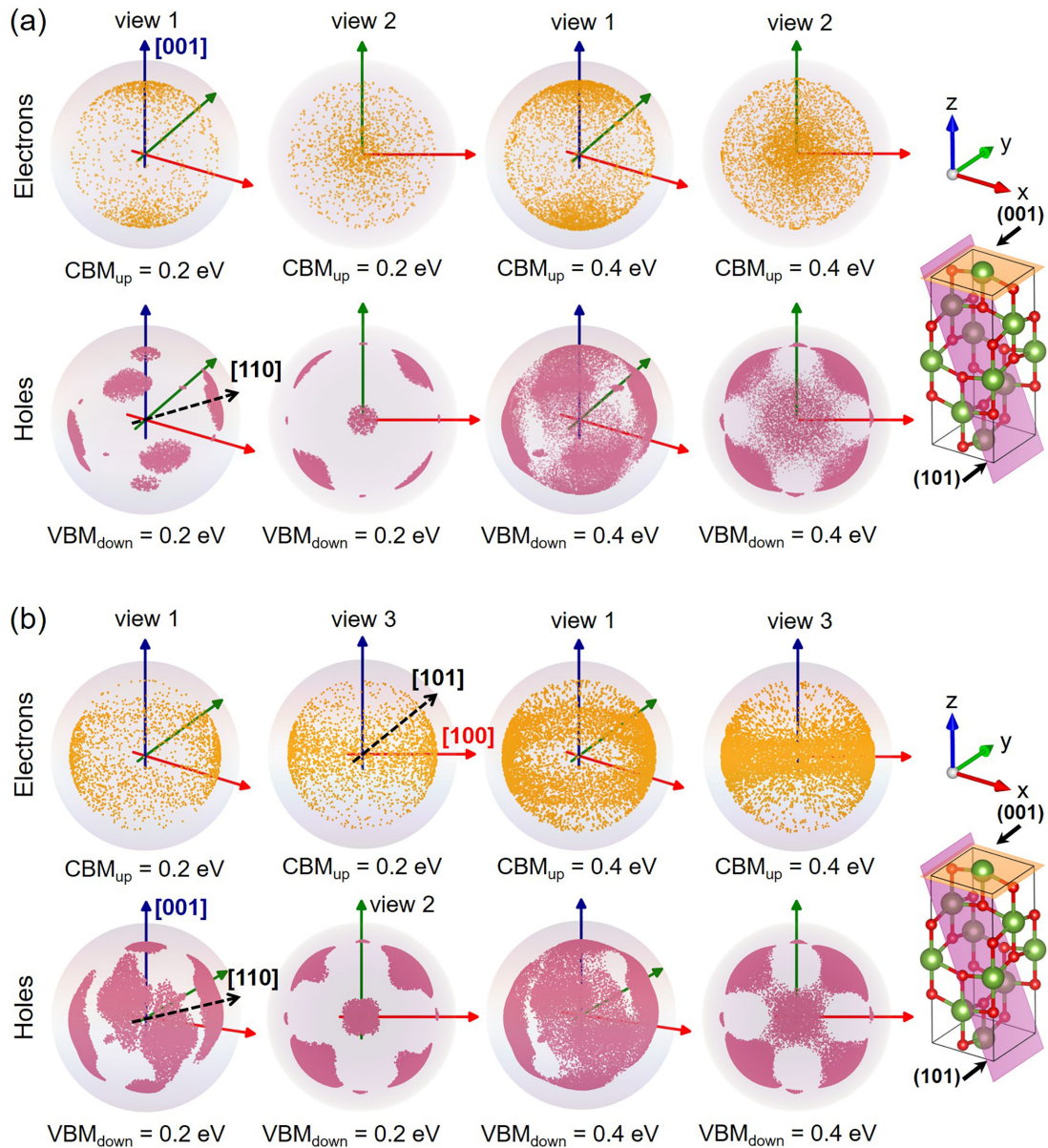


FIG. 8. Photoexcited carrier energy and momentum space distribution (a) and group velocity space distribution (b) in anatase  $\text{TiO}_2$ . The radial coordinate in each panel is the carrier energy relative to the middle of the band gap; the angular coordinates correspond to the carrier momentum and group velocity direction.

where  $m_x^*$ ,  $m_y^*$ , and  $m_z^*$  are coefficients corresponding to the electron and hole rest masses along the main crystal axes, which are generally different.  $\bar{k}_{0,x}$ ,  $\bar{k}_{0,y}$ , and  $\bar{k}_{0,z}$  are the projections of the  $\vec{k}$  vector (at CBM and VBM) on the main crystal axes, and  $\bar{k}_x$ ,  $\bar{k}_y$ , and  $\bar{k}_z$  are projections of the  $\vec{k}$  vector on the main crystal axes.

On the other hand, in nanostructures smaller than the mean free path of carriers, ballistic transport, which preserves the momentum direction, becomes significant compared to diffusive transport. Therefore, to some extent, carrier transport in nanostructures may be judged by its initial momentum distribution described by wave vectors.

Figures 8 and 9 show the results. The small dots in the spherical coordinates represent photoexcited carriers. The

distance from the dot to the origin indicates the energy of the photoexcited carriers relative to the middle of the band gap, and the orientation indicates the momentum direction and group velocity direction of photoexcited carriers. Table II lists  $m_e^*/m_0$  and  $m_h^*/m_0$  along the crystallographic directions of [100], [010], and [001], i.e., the  $x$ ,  $y$ , and  $z$  directions, where  $m_e^*$ ,  $m_h^*$ , and  $m_0$  are the mass of electrons, hole carriers, and free electrons, respectively. Considering the symmetry of anatase and rutile  $\text{TiO}_2$ , the effective masses in the  $x$  and  $y$  directions are the same [21]. In addition, we use the Monkhorst-Pack method to sample the  $k$  points in the first Brillouin zone of the reciprocal space, and then convert the  $k$  points in reciprocal space into real space through coordinate transformation. Since the three lattice vectors of  $\text{TiO}_2$  are perpendicular to each other and are used as the  $XYZ$  coordinate



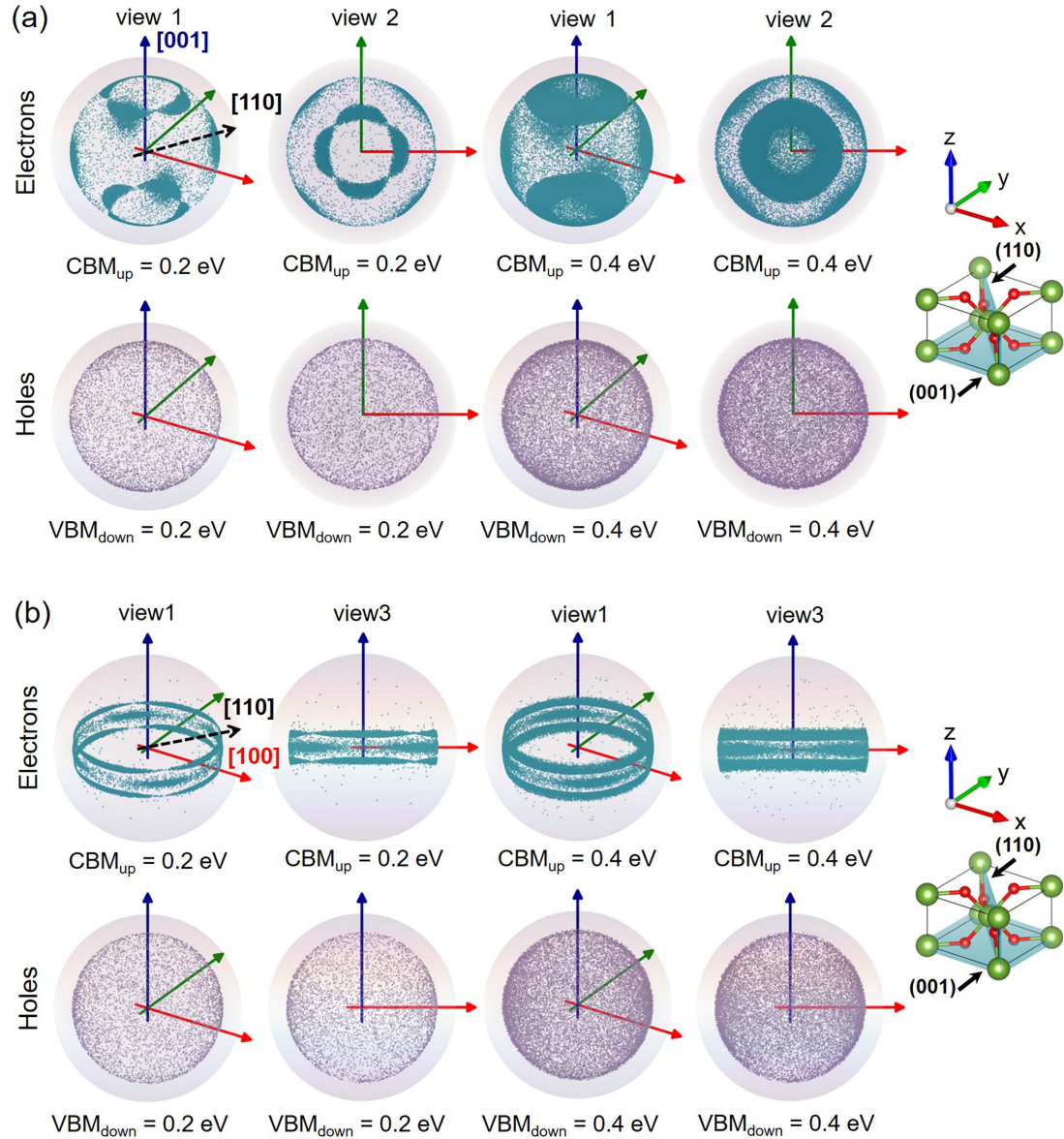


FIG. 9. Photoexcited carrier energy and momentum space distribution (a) and group velocity space distribution (b) in rutile TiO<sub>2</sub>. The radial coordinate in each panel is the carrier energy relative to the middle of the band gap; the angular coordinates correspond to the carrier momentum and group velocity direction.

system, the wave vectors represented by  $k$  points can correspond to the regular crystallographic directions and surfaces.

As shown in Fig. 8, for anatase TiO<sub>2</sub>, the momentum and group velocity distributions of photoexcited carriers are

TABLE II. The effective mass  $m^*$  of electrons and holes for anatase and rutile TiO<sub>2</sub> obtained from *ab initio* calculations.

Species	Effective mass	$m_e^*/m_0$	$m_h^*/m_0$
Anatase [52]	$m_x^*$	0.59	2.33
	$m_y^*$	0.59	2.33
	$m_z^*$	3.70	0.98
Rutile [53]	$m_x^*$	0.77	3.06
	$m_y^*$	0.77	3.06
	$m_z^*$	8.67	4.36

both anisotropic. For momentum distribution, the momentum directions of photoexcited electrons are mainly in the region of [001], the momentum directions of photoexcited holes are mainly in the region of the [110] direction, and the aggregation of holes is stronger than that of electrons. For group velocity distribution, most electrons are mainly concentrated in the [101] and [100] directions; holes tend to concentrate in the [001] and [110] directions. It can be seen that group velocity space has a distortion relative to our momentum space. In addition, these characteristics are maintained within the energy range of 0.2 and 0.4 eV about the conduction and valence band edges. The carrier migration directions can be discussed in the group velocity space. Therefore, the photoexcited electrons mainly migrate along the [101] and [100] directions and may eventually accumulate on the (101) and (100) facets. The photoexcited holes mainly migrate along the

[001] and [110] directions and may eventually accumulate on the (001) facets and (110) facets, with a larger proportion on the (110) facets. This is consistent with the previous experimental observation that electrons mainly accumulate to (101) and holes mainly accumulate to (001) facets of anatase TiO<sub>2</sub> [11–15]. Our research thus offers a unique basic insight into this particular question.

As shown in Fig. 9, for rutile TiO<sub>2</sub>, the momentum directions of most photoexcited electrons are mainly in the region of the [001] and [110] directions, and holes uniformly distribute in all directions of the 4 $\pi$  space. The group velocity directions of most photoexcited electrons are mainly in the region of the [110] and [100] directions, and holes are also uniformly distributed in all directions of the 4 $\pi$  space. Therefore, based on group velocity space, the photoexcited electrons mainly migrate along the [110] and [100] directions and may eventually accumulate on the (110) and (100) facets. The quite uniform distribution of holes in all directions can be attributed to the composition of the valence band edge. As shown in Figs. 2(b) and 2(d), on the one hand, the O 2*p* states near the valence band edge of anatase TiO<sub>2</sub> exhibit a rapid decrease with the increase of energy, while that of the rutile TiO<sub>2</sub> exhibit a slower decrease with energy, indicating a higher degree of localization of O 2*p* states for anatase. On the other hand, the Ti 3*d* states with strong anisotropy located near the valence band edge of anatase are also stronger than that of rutile. These factors ultimately lead to the notable anisotropic distribution of anatase's holes in the momentum space and the relatively uniform distribution of rutile's holes. From the perspective of momentum direction and group velocity direction constraints, the strong and different localization of electrons and holes in anatase TiO<sub>2</sub> will promote their separation in space, thereby reducing their recombination. This may also be the reason that the performance of rutile in optoelectronic applications is not as good as that of anatase.

## E. Transport properties of carriers in energy and momentum space

### 1. Scattering rates of carriers

The transport properties of carriers are crucial for semiconductor-based optoelectronic applications. Theoretically, it is mainly the electron-electron and electron-phonon scattering that dominate the transport properties in semiconductors, and these two scattering rates may prove crucial to designing new strategies for carrier utilization [41,54]. In the following, using density functional theory and many-body perturbation theory, we calculate the imaginary values of the lowest-order electron-electron and electron-phonon [55–57] scattering self-energy in the energy range from –3 to 3 eV by Eqs. (6) and (7) [39,57],

$$\begin{aligned} \text{Im} \sum_{nk}^{e-e} &= \int_{\text{BZ}} \frac{d\mathbf{k}'}{(2\pi)^d} \sum_{n'} \sum_{GG'} \tilde{\rho}_{nk'n'k'}(\mathbf{G}) \tilde{\rho}_{n'k'nk}^*(\mathbf{G}') \\ &\times \frac{4\pi e^2}{|\mathbf{k}' - \mathbf{k} + \mathbf{G}|^2} \text{Im}[\varepsilon_{\mathbf{G}\mathbf{G}'}^{-1}(\mathbf{k}' - \mathbf{k}, \varepsilon_{nk} - \varepsilon_{n'k'})], \end{aligned} \quad (6)$$

$$\begin{aligned} \text{Im} \sum_{nk}^{e-ph} &= \sum_{n'\alpha} \int_{\text{BZ}} \frac{d\mathbf{k}'}{(2\pi)^d} |g_{n'k',nk}^{\mathbf{k}'-\mathbf{k},\alpha}|^2 \\ &\times \text{Im} \left[ \frac{n_{\mathbf{k}'-\mathbf{k},\alpha} + 1 - f_{n'k}}{E_{nk} - E_{n'k'} - \hbar\omega_{\mathbf{k}'-\mathbf{k},\alpha} - i\eta} \right. \\ &\left. + \frac{n_{\mathbf{k}'-\mathbf{k},\alpha} + f_{n'k}}{E_{nk} - E_{n'k'} + \hbar\omega_{\mathbf{k}'-\mathbf{k},\alpha} - i\eta} \right], \end{aligned} \quad (7)$$

where  $\eta$  is a small Lorentzian broadening, and the other terms are the same as that in Eq. (2). The electron-phonon scattering rate  $\Gamma_{nk}^{e-ph}$  is calculated by  $\Gamma_{nk}^{e-ph} = (\frac{2}{\hbar})\text{Im}(\sum_{nk}^{e-ph})$ , and the electron-electron scattering rate  $\Gamma_{nk}^{e-e}$  by  $\Gamma_{nk}^{e-e} = (\frac{2}{\hbar})\text{Im}(\sum_{nk}^{e-e})$ .

Figure 10 exhibits the calculated electron-electron and electron-phonon scattering rates for carriers near the band edge of anatase and rutile TiO<sub>2</sub>. The dispersion in the results of scattering rate is due to the anisotropy of energy states at each energy. For anatase TiO<sub>2</sub>, with the increasing carrier energy, the electron-electron scattering rate gradually increases. On the other hand, the electron-phonon scattering acts as a dominant scattering over the entire energy range, and its trends are similar to the corresponding DOS [see Figs. 2(b) and 2(d)], which is consistent with the fact that DOS reflects the available phase space for electron-phonon scattering [57,58]. For the rutile TiO<sub>2</sub>, we can also obtain a similar conclusion as for anatase TiO<sub>2</sub>. Notably, from the perspective of holes, the transport capacity for both anatase and rutile TiO<sub>2</sub> is comparable, with the electron-phonon scattering rates being as high as 0.5 fs<sup>-1</sup> at the edge of valence band; from the perspective of electrons, rutile TiO<sub>2</sub> has much stronger electron-phonon scattering at the edge of the conduction band than anatase TiO<sub>2</sub>, which means that anatase TiO<sub>2</sub> has significantly better electron transport capacity than rutile TiO<sub>2</sub>. Note that the electron-phonon scattering rate near the conduction band for both anatase and rutile TiO<sub>2</sub> is consistent with recent results reported by Lian *et al.* [59].

### 2. Relaxation time and the mean free path (MFP) of carriers

Carriers with long relaxation time and mean free path (MFP) are particularly preferred in optoelectronic applications of semiconductors. In the following, the relaxation time and MFP of carriers in anatase and rutile TiO<sub>2</sub> under the combined action of electron-electron and electron-phonon scattering are calculated according to Eqs. (8) and (9).

$$\tau_{nk} = \frac{\hbar}{2\left(\text{Im} \sum_{nk}^{e-ph} + \text{Im} \sum_{nk}^{e-e}\right)}, \quad (8)$$

$$\lambda_{nk} = v_{nk} \tau_{nk}, \quad (9)$$

where  $\tau_{nk}$  and  $v_{nk}$  are the lifetime and group velocity of the carriers of the electronic state  $n\mathbf{k}$ , respectively.

From Figs. 11(a) and 11(b), the carriers at energy near the band edges have similar longest relaxation times  $\sim 10$ –15 fs, and decay rapidly at energies roughly 0.5 eV away from the band edges. Figures 11(c) and 11(d) show MFP for both electrons and holes in anatase and rutile TiO<sub>2</sub>. The MFP distribution of electrons and holes are similar to the relaxation time. It is worth noting that the electrons in anatase

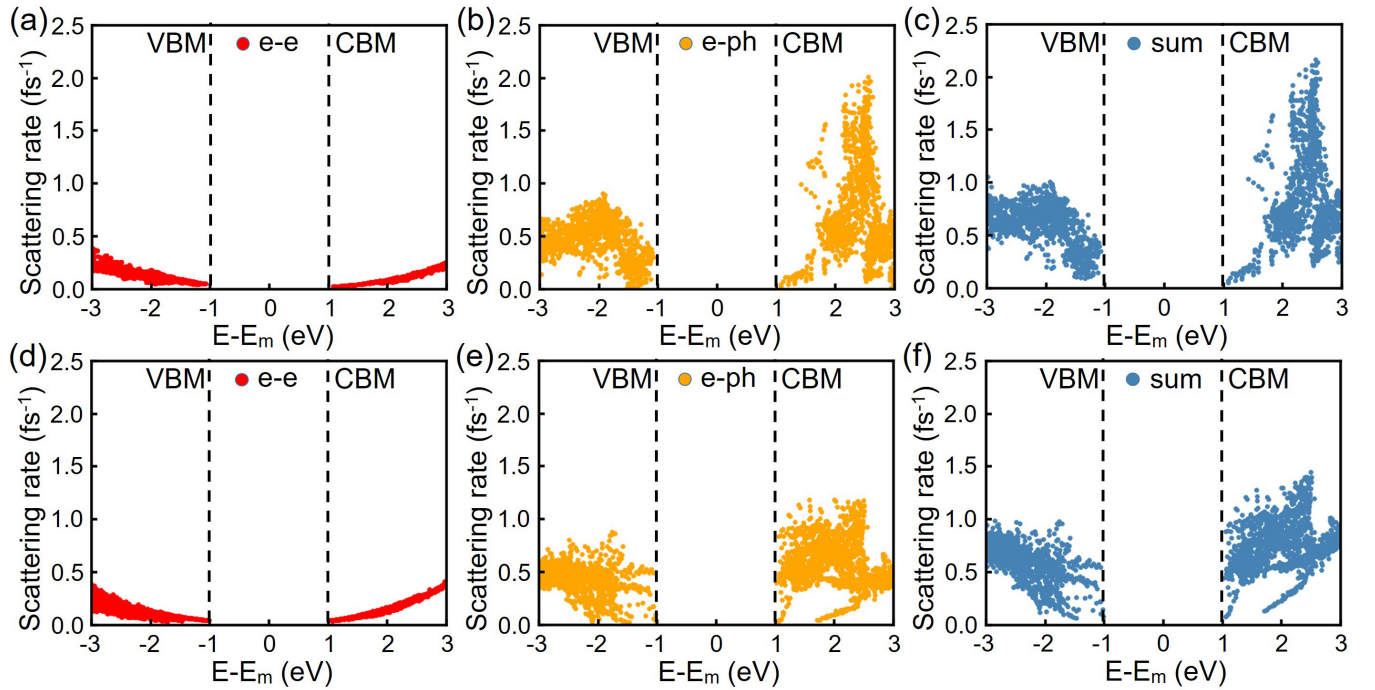


FIG. 10. Electron-phonon and electron-electron scattering rate for anatase (a)–(c) and rutile (d)–(f). The black dashed lines indicate the position of VBM and CBM, and the center of the band gap ( $E_m$ ) is set to 0 eV.

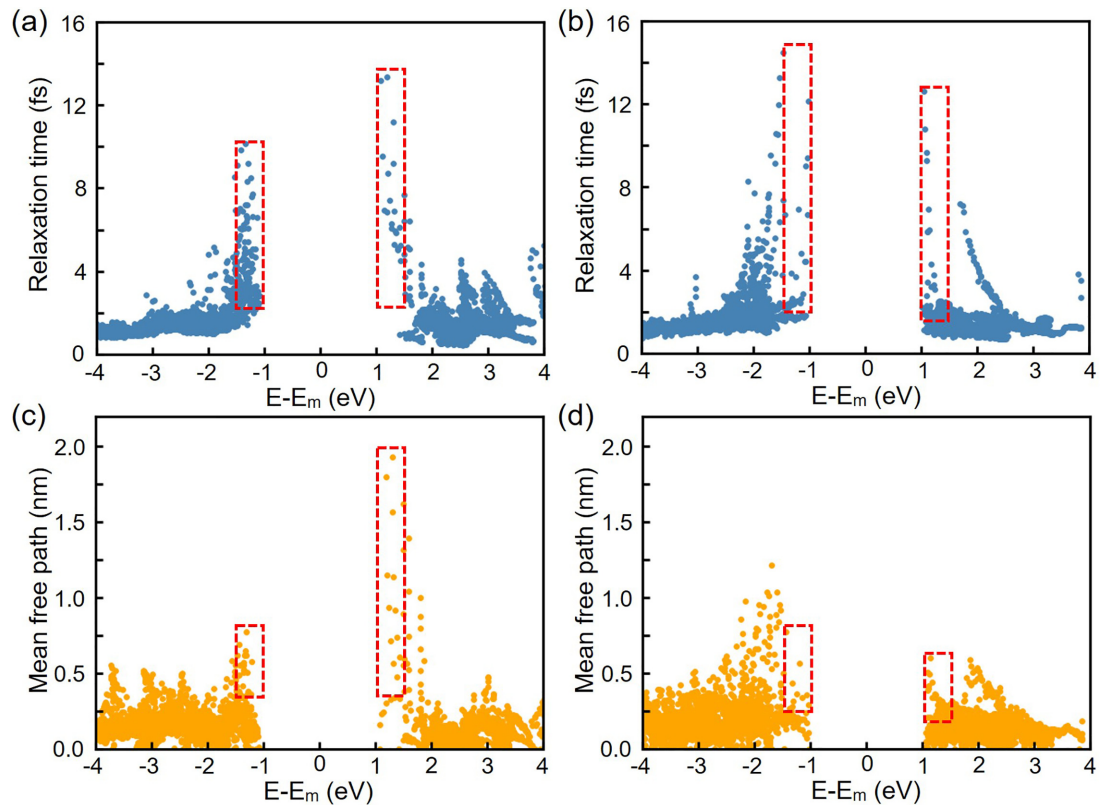


FIG. 11. Carrier relaxation time and MFP as a function of energy. (a), (c) anatase, (b), (d) rutile. Negative values are for photoexcited holes and positive values are for photoexcited electrons.  $E_m$  indicates the center of the band gap.



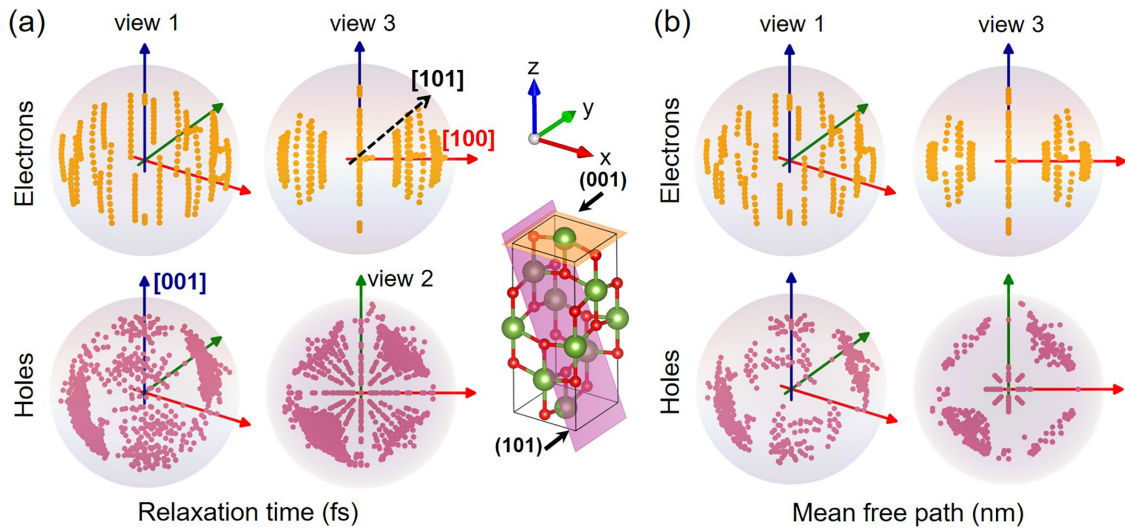


FIG. 12. Relaxation time (a) and MFP (b) as a function of energy and group velocity direction for photoexcited electrons and holes in anatase  $\text{TiO}_2$ . The radial coordinate in each panel is the carrier energy relative to the middle of the band gap, while the angular coordinates correspond to the carrier group velocity directions.

$\text{TiO}_2$  have the longest MFP  $\sim 2$  nm near the energy band edge and are about three times longer than that of rutile  $\text{TiO}_2$ . This corresponds to the fact that rutile  $\text{TiO}_2$  has much stronger electron-phonon scattering at the edge of the conduction band than anatase  $\text{TiO}_2$ . Near the band edge, the electrons in anatase  $\text{TiO}_2$  have a larger relaxation time and MFP than holes, while the situation is exactly the opposite in rutile  $\text{TiO}_2$ .

In order to show the optimal transport direction of electrons and holes near the band edge, we draw the relaxation time and MFP distribution in the group velocity space for energy states enclosed by the red dashed box in Fig. 11. Among them, the radial coordinate in each panel is carrier energy relative to the middle of the band gap, the angular coordinates correspond to the carrier group velocity direction.

For anatase  $\text{TiO}_2$ , as shown in Fig. 12, the group velocity direction of photoexcited electrons with longer relaxation time and MFP are mainly concentrated in the [101] and [100] directions, with holes mainly concentrated in the [001] and [110] directions. It is worth noting that the crystal directions with excellent transport properties are consistent with the initial group velocity distribution in anatase  $\text{TiO}_2$ , indicating beneficial transport and accumulation of photoexcited carriers. This is essential for anatase  $\text{TiO}_2$  to exhibit excellent photoelectric properties. For rutile  $\text{TiO}_2$ , as shown in Fig. 13, the group velocity direction of photoexcited electrons with longer relaxation time and MFP are mainly concentrated in the [110] and [100] directions, with holes mainly concentrated in the [001] and [110] directions. Particularly, for holes of rutile  $\text{TiO}_2$ , the crystal directions with excellent transport proper-

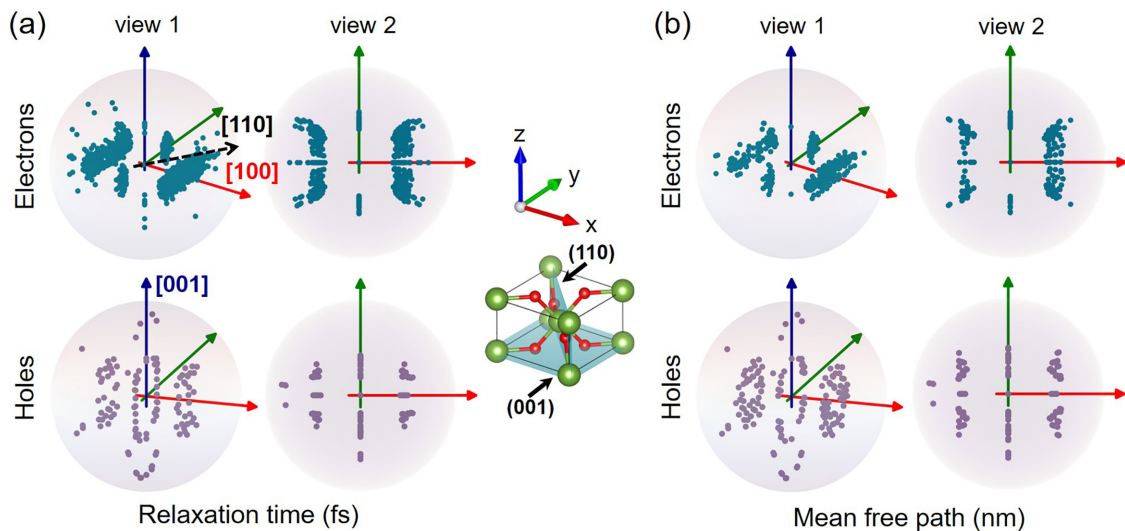


FIG. 13. Relaxation time (a) and MFP (b) as a function of energy and group velocity direction for photoexcited electrons and holes in rutile  $\text{TiO}_2$ . The radial coordinate in each panel is the carrier energy relative to the middle of the band gap, while the angular coordinates correspond to the carrier group velocity directions.

ties are inconsistent with the initial group velocity directions. That is, there is a mismatch between the uniformity of the initial group velocity distribution and the nonuniformity of the transport characteristics, which will lead to poor utilization of holes. On the other hand, the energy states of the electrons are distributed in the crystal directions with excellent transport properties, which is beneficial to the transport and accumulation of electrons. Consequently, because the utilization of electrons is better than that of holes, an important limiting factor for the application of rutile TiO<sub>2</sub> lies in the holes.

#### IV. CONCLUSION

In summary, we have systematically studied the initial energy, momentum, group velocity distributions, and spatial transport properties of photoexcited carriers for both anatase and rutile TiO<sub>2</sub>. The distribution of the photoexcited carriers in the energy space shows that anatase and rutile TiO<sub>2</sub> mainly produce high-energy electrons and holes, respectively, which is beneficial for the efficient separation of carriers in the heterojunction system of anatase and rutile TiO<sub>2</sub>. In addition, it is found that for both anatase and rutile TiO<sub>2</sub>, the initial momentum and group velocity distribution of the photoexcited carriers are highly anisotropic,

and anatase TiO<sub>2</sub> has a better directionality than rutile as a whole. Moreover, the transport properties of carriers in group velocity space also exhibit high anisotropy. Notably, the crystal directions with excellent transport properties are consistent with the momentum and group velocity distribution of carriers in anatase TiO<sub>2</sub>, which indicates beneficial transport and accumulation of photoexcited carriers. In contrast, the crystal directions with excellent transport properties are inconsistent with the preferable group velocity distribution of carriers in rutile TiO<sub>2</sub>, which may result in unfavorable carrier transport and accumulation properties, and this deficiency is especially notable for holes. These results provide insights into the photoelectronic properties of different TiO<sub>2</sub> phases, crystal directions, and facets. The proposed perspectives and frameworks can be exploited for characterizing the crystal direction and facet-dependent photoelectric properties of other materials.

#### ACKNOWLEDGMENTS

This work is supported by the Natural Science Basic Research Program of Shaanxi (Program No. 2022JZ-04), and the National Natural Science Foundation of China (Grant No. 61904138).

- 
- [1] A. Fujishima, X. Zhang, and D. Tryk, TiO<sub>2</sub> photocatalysis and related surface phenomena, *Surf. Sci. Rep.* **63**, 515 (2008).
- [2] J. Schneider, M. Matsuoka, M. Takeuchi, J. Zhang, Y. Horiuchi, M. Anpo, and D. W. Bahnemann, Understanding TiO<sub>2</sub> photocatalysis: Mechanisms and materials, *Chem. Rev.* **114**, 9919 (2014).
- [3] M. M. Khan, S. F. Adil, and A. Al-Mayouf, Metal oxides as photocatalysts, *J. Saudi Chem. Soc.* **19**, 462 (2015).
- [4] Y. Wang, H. Sun, S. Tan, H. Feng, Z. Cheng, J. Zhao, A. Zhao, B. Wang, Y. Luo, J. Yang *et al.*, Role of point defects on the reactivity of reconstructed anatase titanium dioxide (001) surface, *Nat. Commun.* **4**, 2214 (2013).
- [5] J. Wang, H. Sun, J. Huang, Q. Li, and J. Yang, Band structure tuning of TiO<sub>2</sub> for enhanced photoelectrochemical water splitting, *J. Phys. Chem. C* **118**, 7451 (2014).
- [6] J. Yu, J. Low, W. Xiao, P. Zhou, and M. Jaroniec, Enhanced photocatalytic CO<sub>2</sub>-reduction activity of anatase TiO<sub>2</sub> by co-exposed 001 and 101 facets, *J. Am. Chem. Soc.* **136**, 8839 (2014).
- [7] E. Pližingrová, M. Klementová, P. Bezdička, J. Boháček, Z. Barbieriková, D. Dvoranová, M. Mazúr, J. Krýsa, J. Šubrt, and V. Brezová, 2D-Titanium dioxide nanosheets modified with Nd, Ag and Au: Preparation, characterization and photocatalytic activity, *Catal. Today* **281 Part 1**, 165 (2017).
- [8] Y. Shi, H. Sun, M. C. Nguyen, C. Wang, K. Ho, W. A. Saidi, and J. Zhao, Structures of defects on anatase TiO<sub>2</sub>(001) surfaces, *Nanoscale* **9**, 11553 (2017).
- [9] M. A. Henderson, A surface science perspective on TiO<sub>2</sub> photocatalysis, *Surf. Sci. Rep.* **66**, 185 (2011).
- [10] A. V. Akimov, A. J. Neukirch, and O. V. Prezhdo, Theoretical insights into photoinduced charge transfer and catalysis at oxide interfaces, *Chem. Rev.* **113**, 4496 (2013).
- [11] T. Tachikawa, S. Yamashita, and T. Majima, Evidence for crystal-face-dependent TiO<sub>2</sub> photocatalysis from single-molecule imaging and kinetic analysis, *J. Am. Chem. Soc.* **133**, 7197 (2011).
- [12] Q. Tay, X. Liu, Y. Tang, Z. Jiang, T. C. Sum, and Z. Chen, Enhanced photocatalytic hydrogen production with synergistic two-phase anatase/brookite TiO<sub>2</sub> nanostructures, *J. Phys. Chem. C* **117**, 14973 (2013).
- [13] X. Wang, T. Li, R. Yu, H. Yu, and J. Yu, Highly efficient TiO<sub>2</sub> single-crystal photocatalyst with spatially separated Ag and F<sup>-</sup> bi-cocatalysts: Orientation transfer of photogenerated charges and their rapid interfacial reaction, *J. Mater. Chem. A* **4**, 8682 (2016).
- [14] M. Kus, T. Altantzis, S. Vercauteren, I. Caretti, O. Leenaerts, K. J. Batenburg, M. Mertens, V. Meynen, B. Partoens, S. Van Doorslaer *et al.*, Mechanistic insight into the photocatalytic working of fluorinated anatase {001} nanosheets, *J. Phys. Chem. C* **121**, 26275 (2017).
- [15] S. Kashiwaya, T. Toupance, A. Klein, and W. Jaegermann, Fermi level positions and induced band bending at single crystalline anatase (101) and (001) surfaces: Origin of the enhanced photocatalytic activity of facet engineered crystals, *Adv. Energy Mater.* **8**, 1802195 (2018).
- [16] X. Zhao, W. Jin, J. Cai, J. Ye, Z. Li, Y. Ma, J. Xie, and L. Qi, Shape- and size-controlled synthesis of uniform anatase TiO<sub>2</sub> nanocuboids enclosed by active {100} and {001} facets, *Adv. Funct. Mater.* **21**, 3554 (2011).
- [17] T. R. Gordon, M. Cargnello, T. Paik, F. Mangolini, R. T. Weber, P. Fornasiero, and C. B. Murray, Nonaqueous synthesis of TiO<sub>2</sub> nanocrystals using TiF<sub>4</sub> to engineer morphology, oxygen vacancy concentration, and photocatalytic activity, *J. Am. Chem. Soc.* **134**, 6751 (2012).

- [18] E. Bae and T. Ohno, Exposed crystal surface-controlled rutile TiO<sub>2</sub> nanorods prepared by hydrothermal treatment in the presence of poly(vinyl pyrrolidone), *Appl. Catal. B* **91**, 634 (2009).
- [19] G. Liu, H. G. Yang, J. Pan, Y. Q. Yang, G. Q. Lu, and H. M. Cheng, Titanium dioxide crystals with tailored facets, *Chem. Rev.* **114**, 9559 (2014).
- [20] Q. Zhang, R. Li, Z. Li, A. Li, S. Wang, Z. Liang, S. Liao, and C. Li, The dependence of photocatalytic activity on the selective and nonselective deposition of noble metal cocatalysts on the facets of rutile TiO<sub>2</sub>, *J. Catal.* **337**, 36 (2016).
- [21] J. Zhang, P. Zhou, J. Liu, and J. Yu, New understanding of the difference of photocatalytic activity among anatase, rutile and brookite TiO<sub>2</sub>, *Phys. Chem. Chem. Phys.* **16**, 20382 (2014).
- [22] G. Di Liberto, S. Tosoni, and G. Pacchioni, Role of heterojunction in charge carrier separation in coexposed anatase (001)-(101) surfaces, *J. Phys. Chem. Lett.* **10**, 2372 (2019).
- [23] Y. F. Li and Z. P. Liu, Particle size, shape and activity for photocatalysis on titania anatase nanoparticles in aqueous surroundings, *J. Am. Chem. Soc.* **133**, 15743 (2011).
- [24] J. Zhang, T. F. Hughes, M. Steigerwald, L. Brus, and R. A. Friesner, Realistic cluster modeling of electron transport and trapping in solvated TiO<sub>2</sub> nanoparticles, *J. Am. Chem. Soc.* **134**, 12028 (2012).
- [25] S. Selcuk and A. Selloni, Facet-dependent trapping and dynamics of excess electrons at anatase TiO<sub>2</sub> surfaces and aqueous interfaces, *Nat. Mater.* **15**, 1107 (2016).
- [26] C. A. Walenta, M. Tschurl, and U. Heiz, Introducing catalysis in photocatalysis: What can be understood from surface science studies of alcohol photoreforming on TiO<sub>2</sub>, *J. Phys.: Condens. Matter* **31**, 473002 (2019).
- [27] R. Sundararaman, K. Letchworth-Weaver, K. A. Schwarz, D. Gunceler, Y. Ozhabes, and T. A. Arias, JDFTx: Software for joint density-functional theory, *SoftwareX* **6**, 278 (2017).
- [28] N. Marzari, A. A. Mostofi, J. R. Yates, I. Souza, and D. Vanderbilt, Maximally localized Wannier functions: Theory and applications, *Rev. Mod. Phys.* **84**, 1419 (2012).
- [29] M. Horn, C. F. Schwebdfeger, and E. P. Meagher, Refinement of the structure of anatase at several temperatures, *Z. Kristallogr. - Cryst. Mater.* **136**, 273 (1972).
- [30] T. M. Sabine and C. J. Howard, Determination of the oxygen  $x$  parameter in rutile by neutron powder methods, *Acta Crystallogr., Sect. B: Struct. Crystallogr. Cryst. Chem.* **38**, 701 (1982).
- [31] C. Di Valentin, G. Pacchioni, and A. Selloni, Theory of carbon doping of titanium dioxide, *Chem. Mater.* **17**, 6656 (2005).
- [32] T. Zhu and S.-P. Gao, The stability, electronic structure, and optical property of TiO<sub>2</sub> polymorphs, *J. Phys. Chem. C* **118**, 11385 (2014).
- [33] M. Landmann, E. Rauls, and W. G. Schmidt, The electronic structure and optical response of rutile, anatase and brookite TiO<sub>2</sub>, *J. Phys.: Condens. Matter* **24**, 195503 (2012).
- [34] C.-c. Jian, J. Zhang, W. He, and X. Ma, Au-Al intermetallic compounds: A series of more efficient LSPR materials for hot carriers-based applications than noble metal Au, *Nano Energy* **82**, 105763 (2021).
- [35] S. Schöche, T. Hofmann, R. Korlacki, T. E. Tiwald, and M. Schubert, Infrared dielectric anisotropy and phonon modes of rutile TiO<sub>2</sub>, *J. Appl. Phys.* **113**, 164102 (2013).
- [36] Y. N. Wu, J. K. Wuenschell, R. Fryer, W. A. Saidi, P. Ohodnicki, B. Chorpening, and Y. Duan, Theoretical and experimental study of temperature effect on electronic and optical properties of TiO<sub>2</sub>: Comparing rutile and anatase, *J. Phys.: Condens. Matter* **32**, 405705 (2020).
- [37] A. M. Brown, R. Sundararaman, P. Narang, W. A. Goddard III, and H. A. Atwater, Nonradiative Plasmon Decay and hot carrier dynamics: Effects of phonons, surfaces, and geometry, *ACS Nano* **10**, 957 (2016).
- [38] A. Habib, F. Florio, and R. Sundararaman, Hot carrier dynamics in plasmonic transition metal nitrides, *J. Opt.* **20**, 064001 (2018).
- [39] T. Rangel, D. Kecik, P. E. Trevisanutto, G. M. Rignanese, H. Van Swygenhoven, and V. Olevano, Band structure of gold from many-body perturbation theory, *Phys. Rev. B* **86**, 125125 (2012).
- [40] S. Mukherjee, F. Libisch, N. Large, O. Neumann, L. V. Brown, J. Cheng, J. B. Lassiter, E. A. Carter, P. Nordlander, and N. J. Halas, Hot electrons do the impossible: Plasmon-induced dissociation of H<sub>2</sub> on Au, *Nano Lett.* **13**, 240 (2013).
- [41] Y. C. Lai, H. J. Tsai, C. I. Hung, H. Fujishiro, T. Naito, and W. K. Hsu, Carbon nanotubes enhanced Seebeck coefficient and power factor of rutile TiO<sub>2</sub>, *Phys. Chem. Chem. Phys.* **17**, 8120 (2015).
- [42] S. Gong and B.-G. Liu, Electronic structures and optical properties of TiO<sub>2</sub>: Improved density-functional-theory investigation, *Chin. Phys. B* **21**, 057104 (2012).
- [43] M. H. Samat, A. M. M. Ali, M. F. M. Taib, O. H. Hassan, and M. Z. A. Yahya, Hubbard  $U$  calculations on optical properties of 3d transition metal oxide TiO<sub>2</sub>, *Results Phys.* **6**, 891 (2016).
- [44] E. Baldini, T. Palmieri, A. Dominguez, A. Rubio, and M. Chergui, Giant exciton Mott density in anatase TiO<sub>2</sub>, *Phys. Rev. Lett.* **125**, 116403 (2020).
- [45] K. S. B. De Silva, A. Gentle, M. Arnold, V. J. Keast, and M. B. Cortie, Dielectric function and its predicted effect on localized plasmon resonances of equiatomic Au-Cu, *J. Phys. D: Appl. Phys.* **48**, 215304 (2015).
- [46] X. Huang, T. R. Paudel, S. Dong, and E. Y. Tsymbal, Hexagonal rare-earth manganites as promising photovoltaics and light polarizers, *Phys. Rev. B* **92**, 125201 (2015).
- [47] C. C. Jian, J. Zhang, and X. Ma, Cu-Ag alloy for engineering properties and applications based on the LSPR of metal nanoparticles, *RSC Adv.* **10**, 13277 (2020).
- [48] S. Khaleghi, Calculation of electronic and optical properties of doped titanium dioxide nanostructure, *J. Nanostruct.* **2**, 157 (2012).
- [49] R. Sundararaman, P. Narang, A. S. Jermyn, W. A. Goddard III, and H. A. Atwater, Theoretical predictions for hot-carrier generation from surface plasmon decay, *Nat. Commun.* **5**, 5788 (2014).
- [50] F. J. P. Perdew and M. Levy, Physical content of the exact Kohn-Sham orbital energies: Band gaps and derivative discontinuities, *Phys. Rev. Lett.* **51**, 1884 (1983).
- [51] L. Shi and D. Weng, Highly active mixed-phase TiO<sub>2</sub> photocatalysts fabricated at low temperature and the correlation between phase composition and photocatalytic activity, *J. Environ. Sci. (Beijing, China)* **20**, 1263 (2008).



- [52] M. Harb, G. Jeantelot, and J.-M. Basset, Insights into the most suitable  $\text{TiO}_2$  surfaces for photocatalytic  $\text{O}_2$  and  $\text{H}_2$  evolution reactions from DFT calculations, *J. Phys. Chem. C* **123**, 28210 (2019).
- [53] D. Kim, B. C. Yeo, D. Shin, H. Choi, S. Kim, N. Park, and S. S. Han, Dissimilar anisotropy of electron versus hole bulk transport in anatase  $\text{TiO}_2$ : Implications for photocatalysis, *Phys. Rev. B* **95**, 045209 (2017).
- [54] P. Garcia-Goiricelaya, J. Lafuente-Bartolome, I. G. Gurtubay, and A. Eiguren, Long-living carriers in a strong electron-phonon interacting two-dimensional doped semiconductor, *Commun. Phys.* **2**, 81 (2019).
- [55] P. M. Echenique, J. M. Pitarke, E. V. Chulkov, and A. Rubio, Theory of inelastic lifetimes of low-energy electrons in metals, *Chem. Phys.* **251**, 1 (2000).
- [56] M. Xu, J.-Y. Yang, S. Zhang, and L. Liu, Role of electron-phonon coupling in finite-temperature dielectric functions of Au, Ag, and Cu, *Phys. Rev. B* **96**, 115154 (2017).
- [57] M. Bernardi, J. Mustafa, J. B. Neaton, and S. G. Louie, Theory and computation of hot carriers generated by surface plasmon polaritons in noble metals, *Nat. Commun.* **6**, 7044 (2015).
- [58] M. Bernardi, D. Vigil-Fowler, J. Lischner, J. B. Neaton, and S. G. Louie, *Ab initio* study of hot carriers in the first picosecond after sunlight absorption in silicon, *Phys. Rev. Lett.* **112**, 257402 (2014).
- [59] M. Lian, Y.-C. Wang, S. Peng, and Y. Zhao, Photo-induced ultrafast electron dynamics in anatase and rutile  $\text{TiO}_2$ : Effects of electron-phonon interaction, *Chin. J. Chem. Phys.* **35**, 270 (2022).